Tracer-Separator

A Deep Learning Model for Brain PET Dual-Tracer (^{18}F-FDG and Amyloid) Separation

Amirhossein Sanaat, PhD, Yiyi Hu, MSc,* Cecilia Boccalini, PhD,*† Yazdan Salimi, MSc,* Zahra Mansouri, MSc,* Eliluane Pirazzo Andrade Teixeira, MD,* Gregory Mathoux, MD,* Valentina Garibotto, MD,*†‡ and Habib Zaidi, PhD*§||¶*

Introduction: Multiplexed PET imaging revolutionized clinical decision-making by simultaneously capturing various radiotracer data in a single scan, enhancing diagnostic accuracy and patient comfort. Through a transformer-based deep learning, this study underscores the potential of advanced imaging techniques to streamline diagnosis and improve patient outcomes.

Patients and Methods: The research cohort consisted of 120 patients spanning from cognitively unimpaired individuals to those with mild cognitive impairment, dementia, and other mental disorders. Patients underwent various imaging assessments, including 3D T1-weighted MRI, amyloid PET scans using either ^{18}F-florbetapir (FBP) or ^{18}F-flutemetamol (FMM), and ^{18}F-FDG PET. Summed images of FMM/FBP and FDG were used as proxy for simultaneous scanning of 2 different tracers. A SwinUNETR model, a convolution-free transformer architecture, was trained for image translation. The model was trained using mean square error loss function and 5-fold cross-validation. Visual evaluation involved assessing image similarity and amyloid status, comparing synthesized images with actual ones. Statistical analysis was conducted to determine the significance of differences.

Results: Visual inspection of synthesized images revealed remarkable similarity to reference images across various clinical statuses. The mean centiloid bias for dementia, mild cognitive impairment, and healthy control subjects and for FBP tracers is 15.70 ± 29.78, 0.35 ± 33.68, and 6.52 ± 25.19, respectively, whereas for FMM, it is −6.85 ± 25.02, 4.23 ± 23.78, and 5.71 ± 21.72, respectively. Clinical evaluation by 2 readers further confirmed the model's efficiency, with 97 FBP/FMM and 63 FDG synthesized images (from 120 subjects) found similar to ground truth diagnoses (rank 3), whereas 3 FBP/FMM and 15 FDG synthesized images were considered nonsimilar (rank 1). Promising sensitivity, specificity, and accuracy were achieved in amyloid status assessment based on synthesized images, with an average sensitivity of 95 ± 2.5, specificity of 72.5 ± 12.5, and accuracy of 87.5 ± 2.5. Error distribution analyses provided valuable insights into error levels across brain regions, with most falling between −0.1 and +0.2 SUV ratio. Correlation analyses demonstrated strong associations between actual and synthesized images, particularly for FMM images (FBP: Y = 0.72X + 20.95, R^2 = 0.54; FMM: Y = 0.65X + 22.77, R^2 = 0.77).

Conclusions: This study demonstrated the potential of a novel convolution-free transformer architecture, SwinUNETR, for synthesizing realistic FDG and FBP/FMM images from summation scans mimicking simultaneous dual-tracer imaging.

Key Words: PET, neuroimaging, dual-tracer imaging, metabolism, amyloid, deep learning

(*Clin Nucl Med* 2025;50: 1–10)

Multiplexed PET imaging provides complementary information for clinical decision-making by gathering the pharmacological and pathological characteristics related to various radiotracers. This can be achieved in a single scan or through separate scans conducted on different days.[1–6] In the single-scan strategy, different radiotracers can be injected simultaneously or with a short time offset, and then multitracer PET images (either static or dynamic) are broken into each single tracer's information via separation algorithms. Alternatively, separate scans may involve the injection of different radiotracers on different days, with each scan devoted to a specific tracer. This methodology is immune to image misalignment and physiological changes between sequential scans and temporal lag time. Multiplexed PET imaging can be more comfortable for the patient and allows more efficient use of scanning resources by shortening the examination time and thus operational costs.

Overall, separation methods can be categorized into 8 main categories: (1) separation based on differences in half-lives, (2) compartment model (CM)–based signal separation, (3) RTM (reference-tissue model-based dual-tracer separation),[7] (4) basis pursuit,[8] (5) PCA (principal component analysis),[9] (6) GFADS (generalized factor analysis of dynamic sequences),[10] (7) triple coincidence technique,[11] and (8) artificial intelligence (AI)–based models.[12–19] AI-powered algorithms proved particularly promising in a variety of applications in nuclear imaging.[20–23]

Using differences in decay rates of injected radiotracers for separating the signals was first suggested by Huang et al,[24] and its

Received for publication June 28, 2024; revision accepted August 28, 2024.

From the *Division of Nuclear Medicine and Molecular Imaging, Geneva University Hospital, Geneva, Switzerland; †Laboratory of Neuroimaging and Innovative Molecular Tracers (NIMTlab), Geneva University Neurocenter and Faculty of Medicine, University of Geneva, Geneva, Switzerland; ‡CIBM Center for Biomedical Imaging, Geneva, Switzerland; §Department of Nuclear Medicine and Molecular Imaging, University of Groningen, Groningen, the Netherlands; ||Department of Nuclear Medicine, University of Southern Denmark, Odense, Denmark; and ¶University Research and Innovation Center, Óbuda University, Budapest, Hungary.

Conflicts of interest and sources of funding: The authors have no relevant financial or nonfinancial interests to disclose, and the authors have no competing interests to declare that are relevant to the content of this article. V.G. received research support and speaker fees through her institution from GE Healthcare, Siemens Healthineers, Janssen, and Novo Nordisk. H.Z. received research support through his institution from GE Healthcare.

Compliance with ethical standards: This study was performed in line with the principles of the Declaration of Helsinki. Approval was granted by the local ethics committee. Consent forms were waived given the retrospective nature of the study.

Correspondence to: Habib Zaidi, PhD, Division of Nuclear Medicine and Molecular Imaging, Geneva University Hospital, Rue Gabrielle-Perret-Gentil 4, CH-1205, Genève 14, Switzerland. E-mail: habib.zaidi@hug.ch.

Supplemental digital content is available for this article. Direct URL citation appears in the printed text and is provided in the HTML and PDF versions of this article on the journal's Web site (www.nuclearmed.com).

ISSN: 1536-0229/25/5001–0001
DOI: 10.1097/RLU.0000000000005511

application was investigated for separating ^{18}F-FDG and ^{13}N-NH_4^+ in rat brain in the study of cerebral ischemia.[25] Other studies used a similar technique and reported some cons, such as the need for a large difference between the half-lives of the 2 tracers.[26,27] CM-separation method uses the pharmacokinetic models related to each radiotracer and attempts by adjusting the parameters to estimate the time activity curves (TACs) of each tracer, which fit well with the TACs of the dynamic dual-tracer scan.[28] Once the CMs are fitted to the TACs, the signals of the 2 tracers can be separated. The parameters of each CM provide information about the kinetics of each tracer within the region of interest (ROI). The CM-separation method suffers from 2 main limitations: first the high level of noise in separated images, which increases inaccuracy, and second, the need for known arterial input function (AIF) of each tracer, which restricts their application.

Other analytical methods, such as RTM, basis pursuit, PCA, and GFADS, suffer from the long-time delay between the injections, and their accuracy is not optimal. Triple coincidence takes place when a specific radionuclide emits a positron and gamma radiation within a coincidence timing window. These types of coincidences are eliminated in conventional image reconstruction, by limiting the energy window. Recently, Pratt et al[11] developed a reconstruction method in which they include the triple coincidence by widening the acquisition energy windows (350–700 keV) and reconstructing the 2-isotope distributions from the raw data. Their method relied on high-energy resolution detectors.

AI-based methods, including machine learning and deep learning (DL) approaches, reported promising results in several works mostly using simulated or phantom studies. Machine learning–based methods for dual-tracer separation were explored by Ding et al[29] where they separated the TACs of ^{18}F-FDG and ^{68}Ga-DOTATATE for an ROI with a 5-minute delay between injections in comparison to 2 days or more delay in conventional separate scanning. This method uses the temporal information of the measured data for separation and requires information about the AIFs of each tracer. On the other hand, DL methods may offer advantages for signal separation, such as the lack of need for AIFs, relying more on spatial distribution pattern of radiotracers, and faster performance. Several studies used DL for signal separation with[12] and without delay[13,15–17] between injections. Yet, all these studies were based on simulation, phantom, or animal studies.

In this study, we present a transformer-based DL method for separating radiotracers with the same half-life from real clinical brain PET images. The generated images and dual-tracer images were assessed qualitatively and quantitatively. Visual assessment was also performed to evaluate the quality of predicted images in comparison to actual single-tracer PET images.

PATIENTS AND METHODS

Patient Demographics

The research cohort comprised patients referred to Geneva University Hospitals, spanning from cognitively unimpaired/healthy control (HC) individuals to mild cognitive impairment (MCI) and dementia (DEM). Approval was obtained from the local ethics committee (Geneva Canton ethics committee), ensuring adherence to the ethical principles outlined in the Declaration of Helsinki and the good clinical practice standards established by the International Conference on Harmonization. All patients signed informed consent in accordance with specific guidelines.

A total of 120 patients were included in our study and were categorized into the following: HC (n = 18), MCI (n = 72), DEM (n = 21), and other mental disorders (n = 9) following standardized criteria for clinical staging. The inclusion criteria encompassed having at least one 3-dimensional T1-weighted MRI, undergoing dual-phase amyloid PET scans using either ^{18}F-florbetapir (FBP) (n = 63) or ^{18}F-flutemetamol (FMM) (n = 57), undergoing an ^{18}F-FDG PET scan, and having an interval of less than 1 year between imaging assessments.

Table 1 summarizes the demographic and clinical information of our cohort. The mean time intervals between amyloid PET and ^{18}F-FDG PET, between MRI and ^{18}F-FDG PET, and between MRI and amyloid PET were 2.15 months (standard deviation [SD] = 3.06), 1.89 months (SD = 4.15), and 2.76 months (SD = 3.40), respectively. The amyloid status (Aβ+/Aβ−) was determined on late images by an experienced nuclear medicine physician applying the standard operating procedures approved by the European Medicines Agency.

MRI Acquisition

High-resolution anatomical 3D T1 was conducted at Geneva University Hospitals' Division of Radiology on two 3 T MRI scanners (Magnetom Skyra; Siemens Healthineers, Erlangen, Germany and GE Healthcare, Milwaukee, WI) with a matrix size of 256 × 256 and 254 × 254, slice thickness of 0.9 mm and 1 mm, and repetition time of 1930 ms and 7.2 ms, respectively.

PET Acquisition

^{18}F-FDG PET and amyloid brain PET scans were conducted at the Division of Nuclear Medicine and Molecular Imaging of Geneva University Hospitals, utilizing clinical PET scanners, including Biograph 128 mCT, Biograph 128 Vision 600 Edge, Biograph 40 mCT, or Biograph 64 TruePoint (Siemens Healthineers). It is important to note that all scanners had comparable performance. ^{18}F-FDG PET scanning followed the guidelines outlined by the European Association of Nuclear Medicine.[30] For amyloid PET imaging, we

TABLE 1. Demographics of the Dataset Used in This Study Protocol

	Whole Sample	FBP Group	FMM Group	*P*
n	120	63	57	
Age (mean ± SD)	71.47 ± 6.09	72.38 ± 4.75	70.45 ± 7.17	*P* = 0.014
Gender (F/M)	69/51	38/25	31/26	*P* = 0.43
MMSE (mean ± SD)	24.84 ± 4.16	24.86 ± 4.09	24.82 ± 4.20	*P* = 0.442
Aβ status (negative/positive)	70/93	16/47	22/35	*P* = 0.950
Clinical stages (HC/OMD/SCD/MCI/DEM)	18/3/6/72/21	4/1/3/40/15	14/2/3/32/6	*P* = 0.261

The *P* values reported resulted from a *t* test comparing data from the FBP and FMM subgroups.
F, females; M, males; Aβ, amyloid; SCD, subjective cognitive decline; OMD, other mental disorders.

utilized either FBP or FMM. The determination of amyloid status (Aβ+/Aβ−) for each late image was carried out by an experienced nuclear medicine physician, following the standard operating procedures approved by the European Medicines Agency.

MRI and PET Normalization Processing

MRI 3D T1 sequences were registered to the Montreal Neurologic Institute space using 12 degrees of freedom using the Statistical Parametric Mapping (SPM 12), which was executed under MATLAB R2018b, version 9.5 (MathWorks Inc). ^{18}F-FDG and FBP/FMM images were aligned with each subject's T1 MRI and standardized to the Montreal Neurologic Institute space using the transformation matrix from MRI registration. PET images underwent spatial smoothing using 3D 8-mm Gaussian kernel. The procedures conducted were compliant with established protocols.[31]

For the quantification of SUV ratio (SUVR), we employed automated anatomic labeling ROIs. SUVR values were computed by standardizing the uptake within these regions against the combined mean values of the pons and cerebellar vermis, and the whole cerebellum, serving as the reference region for ^{18}F-FDG and FBP/FMM, respectively. The resulting intensity-normalized PET images were saved for subsequent analyses. FBP/FMM SUVR was also extracted from the centiloid volume of interest and converted into centiloid units as recommended by Klunk et al.[32]

SwinUNETR Model Implementation

Inspired from previous literature,[33–35] our investigation introduced a convolution-free transformer architecture (Supplementary Fig. 1, http://links.lww.com/CNM/A508). Transformer-based models, such as SwinUNETR, have shown potential for implementation in clinical setting to address the streamlining workload caused by image segmentation,[3] to enhance image quality and quantitative accuracy,[6,7] to improve the diagnostic confidence,[8] and to increase patient throughput.[9]

Architecture Overview

The Swin Transformer encoder, characterized by its ability to extract feature representations across multiple resolutions utilizing a shifted windowing mechanism[34] for self-attention computation, demonstrated superior efficacy in capturing multiscale contextual representations and addressing long-range dependencies compared with ViT-based methodologies with fixed resolutions. The architectural framework comprises an encoder, bottleneck, decoder, and skip connections.

Encoder

The model processes inputs (summation of FMM/FBP and FDG images) initially dividing them into 3D tokens and projecting them into an embedding space. Self-attention is computed within nonoverlapping windows for efficient token interaction modeling. The shifted windowing mechanism employs window sizes of $M \times M \times M$ to evenly partition tokens at each layer. The encoder features a patch size of $2 \times 2 \times 2$ and a feature dimension of 32. With an embedding space dimension of 24, the encoder comprises 4 stages, each with 2 transformer blocks, totaling 8 layers. Patch merging layers decrease feature representation resolution by a factor of 2 at the end of each stage. Stage 1 uses a linear embedding layer, followed by subsequent stages with similar network designs but different resolutions.

Skip Connections

Skip connections are established between the encoder and decoder to facilitate signal propagation. A bottleneck within the encoder provides an additional link between the encoder and decoder without changing the spatial dimensions of the data.

Decoder

Swin UNETR features a U-shaped network, where encoder features are passed to the decoder via skip connections. At each stage, output features are reshaped and processed through a residual block with two $3 \times 3 \times 3$ convolutional layers normalized by instance normalization. Feature maps are then unsampled by a deconvolutional layer, concatenated with previous stage outputs, and processed by another residual block.

Training and Evaluation

The model is trained using the sum of mean square error (MSE) loss function of FDG and FMM/FBP and a 5-fold cross-validation methodology. Images are kept within the SUVR range without normalization. Training lasts for 300 epochs, stopping when the loss function converges.

Assessment of Image Quality

Initially, the predicted images underwent visual inspection to detect potential artifacts and abnormalities, followed by efforts to identify underlying causes and provide detailed reports for documentation. In our investigation, the assessment of the DL model's performance was conducted by evaluating various metrics, including the structural similarity index (SSIM), root mean squared error (RMSE), and peak signal-to-noise ratio (PSNR). Different types of errors, including the relative error ([predicted − reference]/reference) × 100%, relative absolute error = (|predicted − reference|/reference) × 100%, and absolute error = (predicted − reference), were computed. These metrics were computed between predicted and reference amyloid and ^{18}F-FDG images. Subsequently, the metrics for each section were averaged to yield a comprehensive assessment. A pairwise t test was conducted individually across all groups, employing a predetermined significance level of 0.05. The distributions of SUVR for all regions and patients were visualized by plotting a Bland-Altman graph for both FBP/FMM and ^{18}F-FDG.

Visual Evaluation

To evaluate the performance of our model in clinical setting, in 2 strategies, 2 experienced nuclear medicine physicians (G.M. with over 5 years' experience and E.T. with 3 years' experience in brain PET imaging) evaluated 60 randomly selected subjects as described below.

First Strategy: The Similarity Score (1–3)

The nuclear medicine physicians evaluated the actual and synthesized ^{18}F-FMM/FBP, ^{18}F-FDG all 4, side by side, and assigned a similarity score (1–3) between actual and synthesized images. The scores were defined as follows:

1. No similarity (score 1): The predicted image does not resemble the actual one.
2. Slightly similar (score 2): The predicted image shows partial overlap with the actual image, some important information was missed (important information conferred in the *Discussion* section).
3. Similar (score 3): The predicted image shows substantial overlap with the actual image, the necessary information was preserved.

Second Strategy: The Amyloid Status Diagnosis (Positive or Negative)

Step 1: Evaluating the dual-tracer (Summation) images.

Physicians evaluate only the sum images plus clinical information, such as age and gender, and diagnose positive or negative amyloid status. Our aim is to evaluate if the standalone dual-tracer images can be used for amyloid status estimation.

Step 2: Evaluating ^{18}F-FMM/FBP images separately.

Physicians assess the predicted ^{18}F-FMM/FBP images and estimate the amyloid status based on their observations. As we already had the amyloid status based on the actual ^{18}F-FMM/FBP images, we did not repeat this task.

Statistical Analysis

To evaluate the level of statistical significance between 2 groups, synthetic ^{18}F-FMM/FBP versus reference ^{18}F-FMM/FBP and synthetic ^{18}F-FDG versus reference ^{18}F-FDG, we performed a paired samples *t* test. A *P* value less than 0.05 was used as threshold for statistical significance.

RESULTS

The initial visual inception revealed that our model is capable of synthesizing realistic FDG and FBP/FMM images from the summation (dual-tracer) images. Figure 1 illustrates 4 different subjects, each representing distinct clinical statuses, for FDG, FBP, and FMM tracers. The "Sum" column showcases dual-tracer images, combining FDG with amyloid (FBP and FMM). Ref FDG and Gen FDG denote the reference and generated FDG images, respectively, whereas FDG_Bias denotes the difference map between the reference and generated FDG images. Likewise, Ref Amy and Gen Amy denote the reference and generated Amyloid images, respectively, whereas Amy_Bias indicates the difference map between the reference and generated Amyloid images. Notably, the image range spans from 0 to 3 SUVR, whereas the difference map range falls between −0.2 and +0.2 SUVR. Additionally, other subject-related metrics, including amyloid status, gender, Mini-Mental State Examination (MMSE) scores, and age, are summarized at the top of each panel.

The quantitative metrics, including relative error, relative absolute error, absolute error, SSIM, and PSNR, for amyloid positive and negative subjects and FBP/FMM and FDG radiotracers are summarized in Table 2. The same analysis was performed between synthesized amyloid/FDG and actual amyloid/FDG images separately for different clinical stage groups (HC, MCI, and DEM) and different amyloid radiotracers (Supplementary Table 1, http://links.lww.com/CNM/A508). The absolute error for the generated positive amyloid (FBP: 0.02 ± 0.05 SUVR, FMM: 0.03 ± 0.03 SUVR) and negative amyloid (FBP: 0.00 ± 0.05 SUVR, FMM: −0.01 ± 0.04 SUVR) were smaller than the synthesized FDG images from positive FDG + FBP/FMM (−0.01 ± 0.04 SUVR, −0.00 ± 0.04 SUVR) and negative FDG + FBP/FMM (−0.02 ± 0.03 SUVR, −0.01 ± 0.04 SUVR) (the positive and negative FDG + FBP/FMM represent the dual-tracer generated form positive and negative FBP/FMM cases).

Figure 2 depicts the average map of absolute errors across subjects for FDG and Amyloid (FBP and FMM) PET scans for positive and negative amyloid status. These error maps provide valuable insight into the certainty associated with the generated images, shedding light on potential error levels within specific brain regions. The image range spans from −0.5 to 0.5. The average error maps for all cases and different diagnostic groups are presented in Supplementary Figures 2–5, http://links.lww.com/CNM/A508.

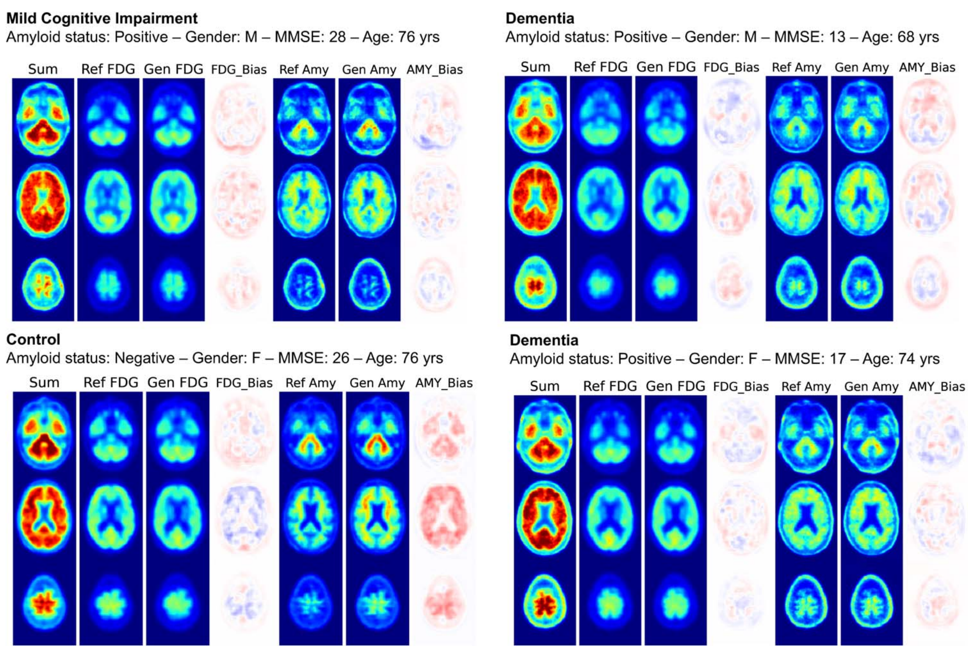

FIGURE 1. Four different subjects depicting various clinical statuses (normal, MCI, DEM) for FDG, FBP, and FMM. The "Sum" column displays dual tracer images (the combined FDG and Amyloid [FBP and FMM]), "Ref FDG" represents the reference FDG, "Gen FDG" denotes the generated FDG, and "FDG_Bias" signifies the difference map between reference and generated FDG. "Ref Amy" represents reference Amyloid, "Gen Amy" refers to generated Amyloid, and "Amy_Bias" indicates the difference map between reference and generated Amyloid. The image range spans from 0 to 3 SUVR, whereas the difference map range is between −0.2 and +0.2 SUVR. Subject-related metrics, including amyloid status, gender, MMSE, and age, are summarized atop each panel.

TABLE 2. The Quantitative Metrics Including FBP and FMM

	Relative Error (%)	Relative Absolute Error (%)	Absolute Error (SUVR)	SSIM	PSNR
Amyloid					
FBP negative					
Mean	−0.67	2.33	0.02	0.88	22.56
SD	2.11	1.27	0.05	0.04	2.34
FBP positive					
Mean	−1.15	3.10	0.00	0.88	22.46
SD	2.77	1.62	0.05	0.03	2.38
FMM negative					
Mean	0.21	1.76	0.03	0.89	22.62
SD	1.16	0.40	0.03	0.03	2.01
FMM positive					
Mean	−1.27	2.82	−0.01	0.91	24.08
SD	2.07	0.99	0.04	0.02	1.35
FDG					
	Relative Error (%)	**Relative Absolute Error (%)**	**Absolute Error (SUVR)**	**SSIM**	**PSNR**
FBP negative					
Mean	−2.18	2.81	−0.02	0.90	21.99
SD	1.69	1.26	0.03	0.02	1.15
FBP positive					
Mean	−1.71	2.78	−0.01	0.89	21.47
SD	2.07	1.35	0.04	0.02	1.38
FMM negative					
Mean	−2.13	3.03	−0.02	0.90	21.81
SD	2.30	1.62	0.04	0.02	1.44
FMM positive					
Mean	−1.44	2.82	0.00	0.88	20.98
SD	2.12	1.06	0.04	0.02	1.48

The PSNR, SSIM, and RMSE were calculated before (^{18}F-FDG vs early phase amyloid) and after (^{18}F-FDG vs pseudo ^{18}F-FDG) using deep learning methods to demonstrate the performance of deep learning for improving the similarity between the ^{18}F-FDG and pseudo ^{18}F-FDG.

Figure 3 shows the visual evaluation of the efficiency of our model for signal separation. From 120 cases reviewed by 2 readers, 97 FBP/FMM and 63 FDG synthesized images were similar to the ground truth, whereas 3 FBP/FMM and 15 FDG synthesized images led to different ratings. Twenty FBP/FMM and 42 FDG images were slightly similar. The readers confirmed that the dual-tracer images were difficult to read because there is a significant difference between the visual evaluation of amyloid and FDG PET scans. An amyloid-negative PET scan shows no cortical fixation of the tracer; however, FDG has physiological cortical fixation, and as such, all summed images would be classified as amyloid-positive. The amyloid status definition by readers based on synthesized FBP/FMM images led to an average sensitivity, specificity, and accuracy of 95 ± 2.5, 72.5 ± 12.5, and 87.5 ± 2.5, respectively (Table 3).

The correlations between the real and synthesized centiloid for FBP (Y = 0.72X + 20.95, R^2 = 0.54) and FMM (Y = 0.65X + 22.77, R^2 = 0.77) are presented in Figure 4. Table 4 also summarizes the SUVR and centiloid bias for HC, MCI, and AD subjects separately. The mean centiloid bias for DEM, MCI, and HC subjects is 15.70 ± 29.78, 0.35 ± 33.68, and 6.52 ± 25.19, respectively, for FBP. It is −6.85 ± 25.02, 4.23 ± 23.78, and 5.71 ± 21.72, respectively, for FMM.

The joint histograms shown in Figure 5 demonstrate the results of a voxel-wise analysis conducted over the test dataset for both FDG and Amyloid radiotracers for different amyloid status. The total and separated joint histograms for HC, MCI, and DEM are illustrated in Supplementary Figures 6–8, http://links.lww.com/CNM/A508.

Figure 6 illustrates the region-wise correlation and Bland-Altman analysis comparing predicted and actual FDG/Amyloid images for different amyloid status. Each data point represents the activity of a specific region for a given subject, with a total of 166 regions calculated across 120 subjects for FDG, FBP, and FMM scans, measured in SUVR units. The total and separated region-wise correlation and Bland-Altman analyses for HC, MCI, and AD were illustrated in Supplementary Figures 9–11, http://links.lww.com/CNM/A508. The generated positive FBP (Y = 0.84X + 0.18, R^2 = 0.71) and positive FDG separated form FDG + FMM (Y = 0.88X + 0.16, R^2 = 0.70) had lowest correlation, whereas negative FMM (Y = 0.91X + 0.01, R^2 = 0.87) and negative FDG separated form FDG + FBP (Y = 1.01X + 0.03, R^2 = 0.79) led to highest correlation.

The results of region-wise absolute error (in SUVR) analysis across 166 brain regions among 120 subjects for both FDG and Amyloid tracers are summarized in Figure 7. The error ranges calculated for bilateral brain regions, mostly fall between −0.1 and +0.2 SUVR. The region-wise absolute error for different diagnostic groups and various radiotracers are depicted in Supplementary Figures 12–14, http://links.lww.com/CNM/A508.

We also conducted subject-wise absolute error analysis to assess the accuracy of FDG and Amyloid imaging across all

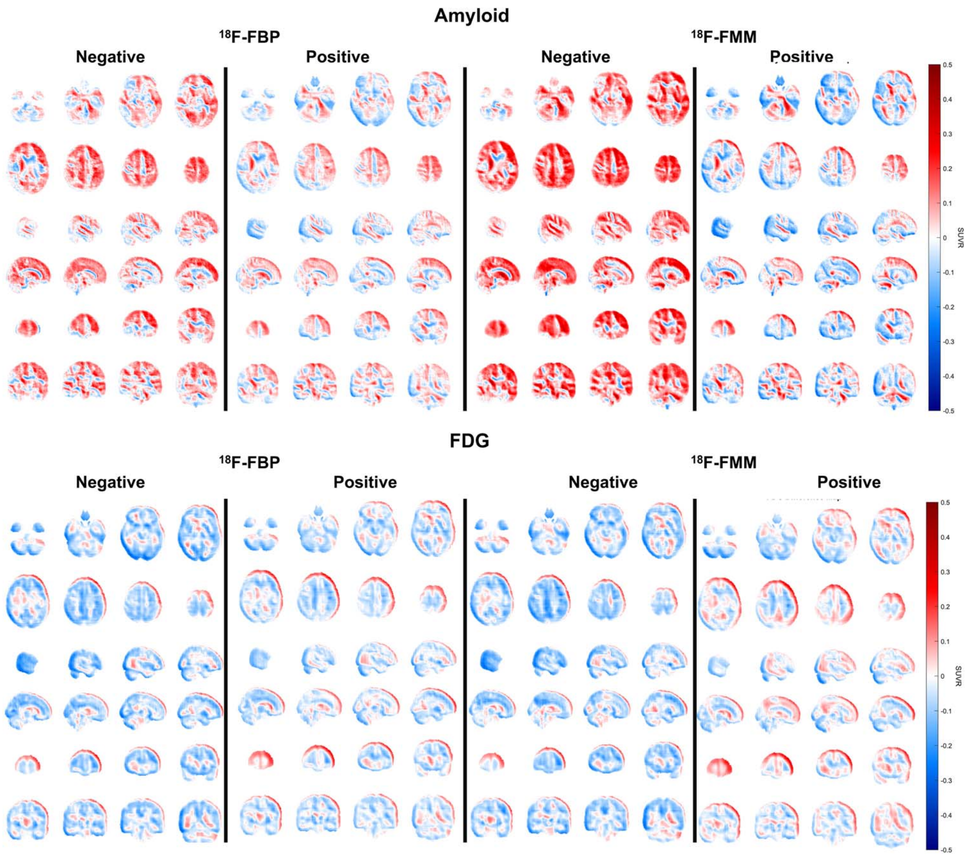

FIGURE 2. Average map of absolute errors across test subjects for synthesized amyloid PET images separated from either FDG + FBP or FDG + FMM for subjects with negative and positive amyloid status. This error map offers insight into the certainty associated with generated images, illustrating potential error levels within specific regions.

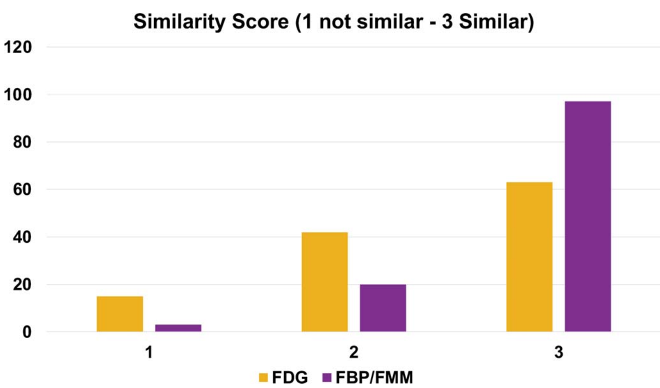

FIGURE 3. Clinical evaluation. The similarity of synthetic FDG and FMM/FBP images separated from dual-tracer images with real FDG and FMM/FBP images. The scores were assigned by 2 experienced nuclear medicine physicians. The synthetic FDG and FMM/FBP images were compared with the corresponding standard of reference FDG images and a similarity score between 1 and 3 assigned. Score 1 indicates lack of any similar information between the synthetic FDG or FMM/FBP images and reference ^{18}F-FDG image, score 2 reflects slightly similar information, whereas score 3 indicates that the 2 images provide similar information and may lead to similar assessment.

120 subjects. The average absolute error in SUVR was calculated over the whole brain for both tracers (Supplementary Figs. 15–18, http://links.lww.com/CNM/A508).

DISCUSSION

Acquiring real-time information about the distribution of 2 different tracers simultaneously is a great opportunity to study the various aspects of brain function and could offer valuable information compared with 2 different separate acquisitions. In addition, simultaneous injection improves patients' comfort and increases scanners throughput. Conventional methods, such as the one described

TABLE 3. The Mean and SD of Sensitivity, Specificity, and Accuracy for Definition of Amyloid Status From Synthesized Amyloid Images, Done by 2 Specialists

	Mean	SD
False positive	5.5	2.5
False negative	2	1
True positive	38	1
True negative	14.5	2.5
Sensitivity	95	2.5
Specificity	72.5	12.5
Accuracy	87.5	2.5

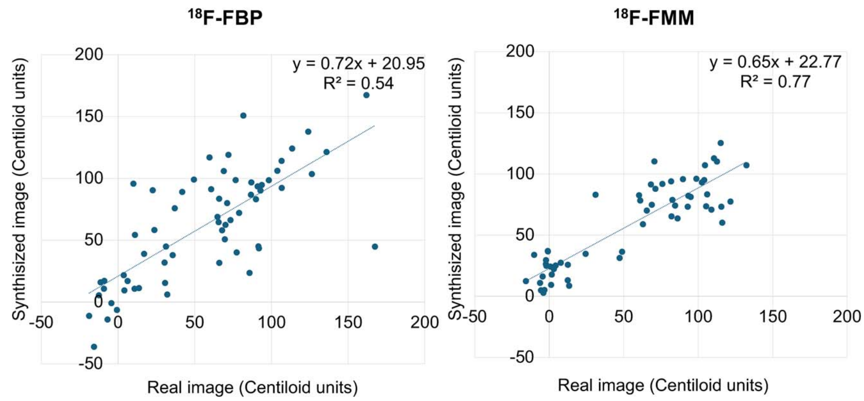

FIGURE 4. The correlation between the real and synthesized FBP and FMM images based on centiloid unit.

TABLE 4. The Calculated SUVR Bias and Centiloid Bias for FBB and FMM

	^{18}F-FBP			
	Mean (SUVR Bias)	**SD (SUVR Bias)**	**Mean (Centiloid Bias)**	**SD (Centiloid Bias)**
DEM	0.09	0.17	15.70	29.78
MCI	0.00	0.19	0.35	33.68
HC	0.04	0.14	6.52	25.19
	^{18}F-FMM			
	Mean (SUVR Bias)	**SD (SUVR Bias)**	**Mean (Centiloid Bias)**	**SD (Centiloid Bias)**
DEM	−0.06	0.21	−6.85	25.02
MCI	0.03	0.20	4.23	23.73
HC	0.05	0.18	5.71	21.72

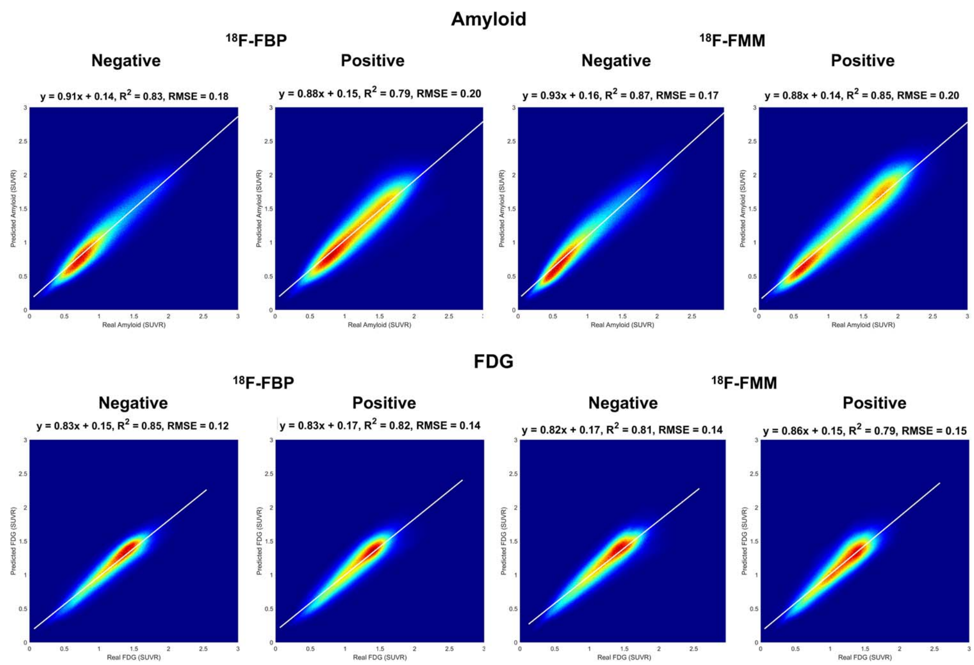

FIGURE 5. The voxel-wise analysis over the test dataset for synthesized amyloid PET images separated from either FDG + FBP or FDG + FMM for positive and negative amyloid status and different tracer groups.

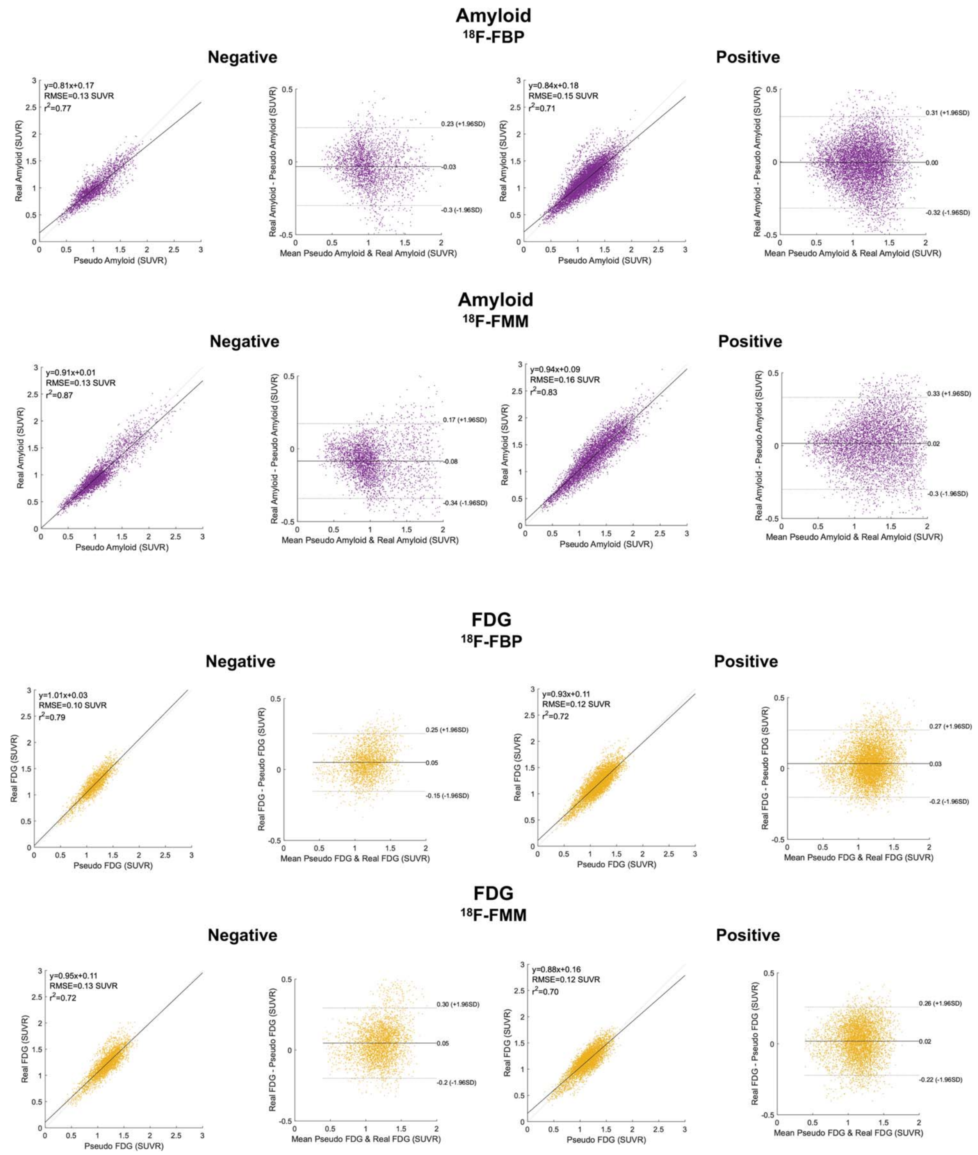

FIGURE 6. Region-wise correlation and Bland-Altman analysis comparing synthesized FDG/Amyloid and real FDG/Amyloid. Each point depicts the activity of a specific region for a given subject. A total of 166 regions were calculated for 120 subject and reported for FDG, FBP, and FMM subjects, measured in SUVR units. In the Bland-Altman graph, the solid black line represents the mean, whereas the dashed lines indicate the upper and lower limits. In the correlation graph, the dashed line serves as the reference line.

in Kadrmas et al,[36] which inject 2 tracers within an interval, do not provide the real-time simultaneous information. Besides, it has been shown that the scanning protocol, injection timing, and tracer combination can affect the results.[19] Strategies were devised to use dynamic images and the TACs pattern to separate 2 signals from 2 tracers in the image domain.[13,17] However, the long acquisition time required for dynamic imaging limits patients' comfort and occupies the scanner for long time in addition to increasing the probability of patients' motion during scanning. Moreover, most approaches require invasive blood sampling and additional information associated with the image information process.

Transformers have shown excellent performance, especially in complex imaging tasks where conventional UNET approaches cannot achieve promising results.[20,37] In this study, we used swinUnetR transformer network to separate 2 signals belonging to 2 different compounds, namely, ^{18}F-FDG and ^{18}F-FBP/FMM, labeled with the same radionuclide (same half-life) using reconstructed static images. As such, long dynamic acquisitions or blood sampling was not required. We used a relatively large number of clinical brain images (120) compared with what is reported in the literature and evaluated the performance of our model extensively using both voxel-wise and region-wise image-derived metrics. Our proposed fully automated methodology uses the summation images and separates 2 ^{18}F-FDG and ^{18}F-FBP/FMM images in a very short time (in the order of seconds), achieving promising results. Unlike former studies that relied mostly on computer simulations,[14,15] we used real clinical studies of patients with possible neurodegenerative diseases referred for brain PET imaging. We

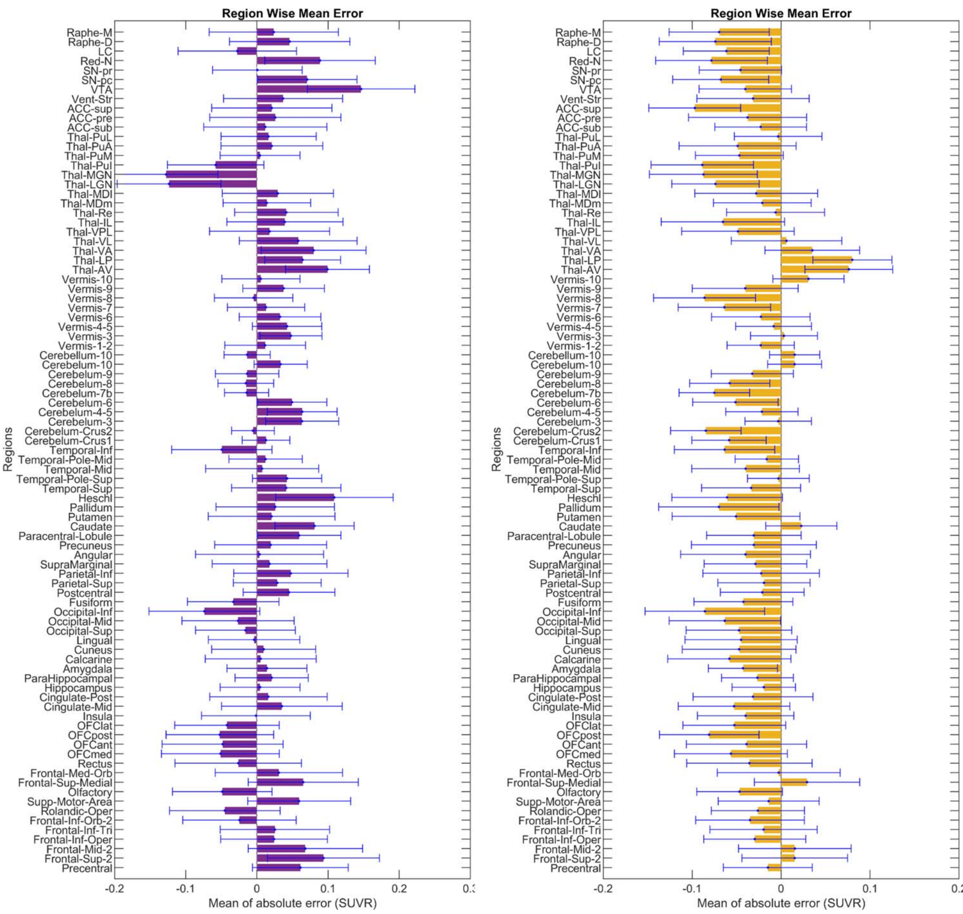

FIGURE 7. Region-wise absolute error analysis. Average of absolute error (SUVR) for each 166 regions between 120 subjects for both FDG and Amyloid were calculated. The average of left and right side was reported for the matter of representation.

managed to register reconstructed brain PET images to a template to circumvent difficulties of registering raw data in the sinogram domain using deformable registration methods that minimize a similarity metric between moving and fixed images. Our methodology showed robust performance on real clinical studies acquired on 4 different scanners with different reconstruction and acquisition parameters for a versatile population with various pathologies (not only normal cases).

In terms of accuracy, our model achieved acceptable performance both in voxel-wise and region-wise analysis. The joint histogram showed a slight underestimation of tracer uptake on Amyloid images with slopes ranging from 0.88 to 0.93, whereas this slope is worse in ^{18}F-FDG separated signal (ranging from 0.82 to 0.86). For most voxels presented in Figure 5, the predicted SUVR is in the range of 95% confidence interval, which along with a voxel-wise relative absolute error of less than 3.03% shows the excellent performance of our model in the test group. In addition, the visual assessment presented in Figure 3 for different cases confirms the very good agreement between the predicted and actual FDG and Amyloid images.

The visual comparative assessment of images included several evaluations starting from a generic assessment of the overall quality of the generated images compared with the actual ones. Subsequently, the presence or absence of hypometabolic regions in ^{18}F-FDG images was assessed. Nuclear medicine physicians assessed the original image and sought the same information on the predicted images.

The same process applies to Amyloid images. First, a general evaluation of the quality of predicted images, followed by an assessment of regions associated with Amyloid status (positive when there is significant cortical fixation). A score of 3 indicates similar images, classified as A+ (or A−) in all regions of interest (frontal, temporal, parietal, occipital, retrosplenial) in both images.

Ruan and Liu[13] used summed sinogram information and neural network to separate 2 images corresponding to ^{11}C-acetate and ^{18}F-FDG compounds. They used simulation studies and reported 0.19 SUV bias in the whole image. In our study, we used real clinical studies and achieved a bias (relative error) of less than 2%.

This study inherently bears some limitations. First, the FMM/FBP and FDG images were acquired separately at different times. We simulated dual-tracer images by summing up images acquired following injection of the 2 tracers. In a clinical scenario, a true dual-tracer image would be obtained following simultaneous injection of both tracers or with minimal delay. Future work will involve assessing our model on actual simultaneously acquired dual-tracer images. The lack of a large dual-tracer clinical dataset, crucial for effective training of DL models, remains the main hurdle.

CONCLUSIONS

We developed a pipeline to separate images of 2 radiopharmaceuticals having the same half-life acquired simultaneously in the reconstructed image domain with an encouraging performance employing state-of-the-art transformer DL models. Our methodology does not require any additional information other than the reconstructed PET images and may be used to separate dual-tracers in clinical setting once the robustness of the methodology can be proved over a larger population.

ACKNOWLEDGMENTS

This work was supported by the Swiss National Science Foundation under grant SNSF 320030_231742. We thank the Centre de la Mémoire of the Geneva University Hospitals for patient inclusion and evaluation. The Centre the la Mémoire is funded by the following private donors under the supervision of the Private Foundation of Geneva University Hospitals: A.P.R.A.–Association Suisse pour la Recherche sur la Maladie d'Alzheimer, Genève, Switzerland; Fondation Segré, Genève, Switzerland; Race Against Dementia Foundation, London, United Kingdom; Fondation Child Care, Genève, Switzerland; Fondation Edmond J. Safra, Genève, Switzerland; Fondation Minkoff, Genève, Switzerland; Fondazione Agusta, Lugano, Switzerland; McCall Macbain Foundation, Canada; Nicole et René Keller, Genève, Switzerland; and Fondation AETAS, Genève, Switzerland. Competitive research projects contributing to data collection have been funded by: H2020 (projects n. 667375), Innovative Medicines Initiative (IMI contract n. 115736 and 115952), IMI2, Swiss National Science Foundation (projects n. 320030_182772, 320030_185028, and n. 320030_169876), and VELUX Foundation. The Clinical Research Centre at Geneva University Hospital and Faculty of Medicine provided valuable support for regulatory submissions and data management.

REFERENCES

1. Ghidaglia J, Golse N, Pascale A, et al. ^{18}F-FDG /^{18}F-choline dual-tracer PET behavior and tumor differentiation in hepatocellular carcinoma. A systematic review. *Front Med (Lausanne)*. 2022;9:924824.
2. Parghane R, Basu S. Small cell transformation of metastatic prostate adenocarcinoma diagnosed by dual-tracer PET/CT ((68)Ga-PSMA and (18)F-FDG): potential clinical utility in therapeutic decision making and treatment monitoring. *J Nucl Med Technol*. 2019;47:85–87.
3. Veenstra EB, Ruiter SJS, de Haas RJ, et al. A dual-tracer approach using [(11)C]CH and [(18)F]FDG in HCC clinical decision making. *EJNMMI Res*. 2023;13:77.
4. Altomare D, Barkhof F, Caprioglio C, et al. Clinical effect of early vs late amyloid positron emission tomography in memory clinic patients: the AMYPAD-DPMS randomized clinical trial. *JAMA Neurol*. 2023;80:548–557.
5. Ianni AM, Eisenberg DP, Boorman ED, et al. PET-measured human dopamine synthesis capacity and receptor availability predict trading rewards and time-costs during foraging. *Nat Commun*. 2023;14:6122.
6. Taheri N, Le Crom B, Bouillot C, et al. Design of a generic method for single dual-tracer PET imaging acquisition in clinical routine. *Phys Med Biol*. 2023;68:085016.
7. Joshi AD, Koeppe RA, Fessier JA, et al. Signal separation and parameter estimation in noninvasive dual-tracer PET scans using reference-region approaches. *J Cereb Blood Flow Metab*. 2009;29:1346–1357.
8. Bell C, Puttick S, Rose S, et al. Design and utilisation of protocols to characterise dynamic PET uptake of two tracers using basis pursuit. *Mol Imaging Biol*. 2017;62:4897–4916.
9. Kadrmas DJ, Rust TC. Feasibility of rapid multitracer PET tumor imaging. *IEEE Trans Nucl Sci*. 2005;52:1341–1347.
10. El Fakhri G, Trott CM, Sitek A, et al. Dual-tracer PET using generalized factor analysis of dynamic sequences. *Mol Imaging Biol*. 2013;15:666–674.
11. Pratt EC, Lopez-Montes A, Volpe A, et al. Simultaneous quantitative imaging of two PET radiotracers via the detection of positron-electron annihilation and prompt gamma emissions. *Nat Biomed Eng*. 2023;7:1028–1039.
12. Pan B, Marsden PK, Reader AJ. Dual-tracer PET image separation by deep learning: a simulation study. *Appl Sci*. 2023;13:4089.
13. Ruan D, Liu H. Separation of a mixture of simultaneous dual-tracer PET signals: a data-driven approach. *IEEE Trans Nucl Sci*. 2017;64:2588–2597.
14. Xu J, Liu H. Three-dimensional convolutional neural networks for simultaneous dual-tracer PET imaging. *Phys Med Biol*. 2019;64:185016.
15. Qing M, Wan Y, Huang W, et al. Separation of dual-tracer PET signals using a deep stacking network. *Nucl Instr Meth A*. 2021;1013:165681.
16. Tong J, Chen Y, Liu H. Single-scan dual-tracer separation network based on pre-trained GRU. In: Li Q, Leahy R, Dong B, et al, eds. *Multiscale Multimodal Medical Imaging*. Cham, Switzerland: Springer International Publishing; 2020:43–50.
17. Xu J, Liu H. Deep-learning-based separation of a mixture of dual-tracer single-acquisition PET signals with equal half-lives: a simulation study. *IEEE Trans Rad Plasma Med Sci*. 2019;3:649–659.
18. Tong J, Wang C, Liu H. Temporal information-guided dynamic dual-tracer PET signal separation network. *Med Phys*. 2022;49:4585–4598.
19. Zeng F, Fang J, Muhashi A, et al. Direct reconstruction for simultaneous dual-tracer PET imaging based on multi-task learning. *EJNMMI Res*. 2023;13:7.
20. Zaidi H, El Naqa I. Quantitative molecular positron emission tomography imaging using advanced deep learning techniques. *Annu Rev Biomed Eng*. 2021;23:249–276.
21. Arabi H, AkhavanAllaf A, Sanaat A, et al. The promise of artificial intelligence and deep learning in PET and SPECT imaging. *Phys Med*. 2021;83:122–137.
22. Jha AK, Bradshaw TJ, Buvat I, et al. Nuclear medicine and artificial intelligence: best practices for evaluation (the RELAINCE guidelines). *J Nucl Med*. 2022;63:1288–1299.
23. Balaji V, Song TA, Malekzadeh M, et al. Artificial intelligence for PET and SPECT image enhancement. *J Nucl Med*. 2024;65:4–12.
24. Huang SC, Carson RE, Hoffman EJ, et al. An investigation of a double-tracer technique for positron computerized tomography. *J Nucl Med*. 1982;23:816–822.
25. Figueiras FP, Jiménez X, Pareto D, et al. Simultaneous dual-tracer PET imaging of the rat brain and its application in the study of cerebral ischemia. *Mol Imaging Biol*. 2011;13:500–510.
26. Kearfott KJ. Feasibility of simultaneous and sequentially administered dual tracer protocols for measurement of regional cerebral haematocrit using positron emission tomography. *Phys Med Biol*. 1990;35:249–258.
27. Verhaeghe J, Asseler YD, Staelens S, et al. Noise properties of simultaneous dual tracer PET imaging. *IEEE Nucl Sci Symp Conference Rec*. 2005;2005:2611–2614.
28. Koeppe RA, Raffel DM, Snyder SE, et al. Dual-[^{11}C]tracer single-acquisition positron emission tomography studies. *J Cereb Blood Flow Metab*. 2001;21:1480–1492.
29. Ding W, Yu J, Zheng C, et al. Machine learning–based noninvasive quantification of single-imaging session dual-tracer (18)F-FDG and (68)Ga-DOTATATE dynamic PET-CT in oncology. *IEEE Trans Med Imaging*. 2022;41:347–359.
30. Guedj E, Varrone A, Boellaard R, et al. EANM procedure guidelines for brain PET imaging using [(18)F]FDG, version 3. *Eur J Nucl Med Mol Imaging*. 2022;49:632–651.
31. Dodich A, Mendes A, Assal F, et al. The a/T/N model applied through imaging biomarkers in a memory clinic. *Eur J Nucl Med Mol Imaging*. 2020;47:247–255.
32. Klunk WE, Koeppe RA, Price JC, et al. The centiloid project: standardizing quantitative amyloid plaque estimation by PET. *Alzheimers Dement*. 2015;11:1–15.e1–4.
33. Cao H, Wang Y, Chen J, et al. Swin-unet: Unet-like pure transformer for medical image segmentation. *arXiv preprint arXiv:210505537*. 2021.
34. Liu Z, Lin Y, Cao Y, et al. Swin transformer: hierarchical vision transformer using shifted windows. *Proc IEEE/CVF Int Conf Comput Vision*. 2021;10012–10022.
35. Dosovitskiy A, Beyer L, Kolesnikov A, et al. An image is worth 16x16 words: transformers for image recognition at scale. *arXiv preprint arXiv:201011929*. 2020.
36. Kadrmas DJ, Rust TC, Hoffman JM. Single-scan dual-tracer FLT + FDG PET tumor characterization. *Mol Imaging Biol*. 2013;58:429–449.
37. Mansouri Z, Salimi Y, Akhavanallaf A, et al. Deep transformer-based personalized dosimetry from SPECT/CT images: a hybrid approach for [^{177}Lu]Lu-DOTATATE radiopharmaceutical therapy. *Eur J Nucl Med Mol Imaging*. 2024;51:1516–1529.